

# A STRUCTURAL-MAGNETIC STRAIN MODEL FOR MAGNETOSTRICTIVE TRANSDUCERS

Marcelo J. Dapino  
Department of Aerospace Engineering  
and Engineering Mechanics  
Iowa State University  
Ames, IA 50011  
marcelod@iastate.edu

Ralph C. Smith  
Center for Research in Scientific Computation  
Department of Mathematics  
North Carolina State University  
Raleigh, NC 27695-8205  
rsmith@eos.ncsu.edu

Alison B. Flatau  
Department of Aerospace Engineering  
and Engineering Mechanics  
Iowa State University  
Ames, IA 50011  
abf@iastate.edu

## Abstract

This paper addresses the modeling of strains generated by magnetostrictive transducers in response to applied magnetic fields. The measured strains are dependent upon both the rotation of moments within the material in response to the field and the elastic properties of the material. The magnetic behavior is characterized through the consideration of the Jiles-Atherton mean field theory for ferromagnetic hysteresis in combination with a quadratic moment rotation model for magnetostriction. The incorporation of elastic properties is necessary to account for the dynamics of the material as it vibrates. This is modeled through force balancing which yields a wave equation with magnetostrictive inputs. The validity of the resulting transducer model is illustrated through comparison with experimental data.

# 1 Introduction

The phenomenon of magnetostriction is characterized by the changes in shape which occur in certain materials when the materials are subjected to magnetic fields. For rare-earth alloys such as Terfenol-D ( $\text{Tb}_{0.3}\text{Dy}_{0.7}\text{Fe}_{1.9}$ ), the generated strains and forces are sufficiently large to prove advantageous in transducer design. Initial investigations have demonstrated the utility of such transducers in applications ranging from ultrasonic transduction to vibration control in heavy structures.

This paper addresses the modeling of strains generated by magnetostrictive materials when employed in transducer design. To illustrate, we consider the prototypical broadband transducer depicted in Figure 1 and detailed in [1]. While transducer design will vary according to specific requirements, this design is typical for control applications and illustrates the various physical components which must be modeled to fully utilize the magnetostrictive actuator capabilities. The primary components of the actuator consist of a cylindrical Terfenol-D rod, a wound wire solenoid, an enclosing permanent magnet and a prestress mechanism. The rod is manufactured so that magnetic moments are primarily oriented perpendicular to the longitudinal axis. The prestress mechanism increases the distribution of moments perpendicular to the rod axis and allows the transducer to be operated in compression. Application of current to the solenoid then produces a magnetic field which causes the moments to rotate so as to align with the field. The resulting strains and forces provide the actuator capabilities for the transducer. The capability for attaining bidirectional strains and forces is provided by a magnetic bias generated by either the surrounding permanent magnet or an applied DC current to the solenoid.

For control applications, it is necessary to accurately quantify the relationship between the current  $I(t)$  applied to the solenoid and the strains  $e(t)$  generated by the transducer. This necessitates modeling the electric, magnetic, mechanical and thermal regimes within the system. While all four regimes are fully coupled, we focus here on the magnetic and mechanical aspects of the system with nearly constant temperatures maintained to reduce thermal effects.

To illustrate the nature of the magnetic and mechanical phenomena, experimental data collected from the transducer depicted in Figure 1 is plotted in Figure 2. In Figure 2a, it is observed that the relationship between the input magnetic field  $H$  and magnetization  $M$  is nonlinear with significant saturation and is irreversible due to hysteresis. These effects must be incorporated when modeling the magnetic regime. The relationship between the magnetization  $M$  and strain  $e$ , plotted in Figure 2b, also exhibits hysteresis and nonlinear features which must be modeled when characterizing the mechanical properties of the system. An important feature of the magnetoelastic model considered here is that it incorporates the observed hysteresis in the strain whereas previously considered models yielded single-valued strain outputs.

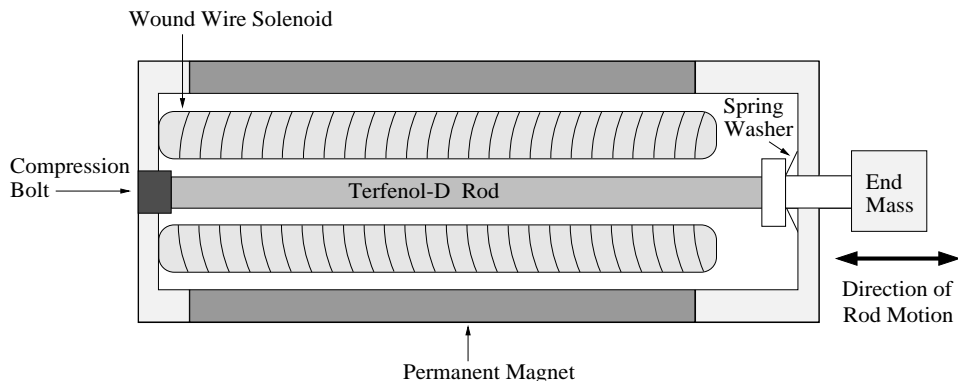


**Figure 1.** Cross section of a prototypical Terfenol-D magnetostrictive transducer.

Initial models quantifying the magnetomechanical coupling were based on the linear constitutive piezomagnetic equations

$$e = s^H \sigma + d_{33} H \quad (1a)$$

$$B = d_{33}^* \sigma + \mu^\sigma H \quad (1b)$$

which are derived from thermodynamic principles in combination with empirical laws. In these relations,  $e$  and  $\sigma$  denote the longitudinal strain and axial stress in the material while  $s^H$  denotes the mechanical compliance at a fixed field strength  $H$ . Moreover,  $B$  and  $\mu^\sigma$  respectively denote the magnetic flux and permeability at constant stress while  $d_{33} \equiv \frac{\partial e}{\partial H}|_\sigma$  and  $d_{33}^* \equiv \frac{\partial B}{\partial \sigma}|_H$  are magnetoelastic coupling coefficients. It is noted in (1a) that the generated strains are dependent upon both the elastic properties of the material (modeled by the term  $s^H \sigma$ ) and magnetic inputs (modeled by  $d_{33} H$ ). Equation (1b) models the converse magnetostrictive effect in which magnetic flux is generated by stresses in the material. This latter property provides the magnetostrictive materials with their sensor capabilities.

While the linear model (1) is commonly employed in magnetostrictive transducer applications, the relations are accurate only at low operating levels. They do not provide mechanisms for incorporating the hysteresis and nonlinearities observed in the data in Figure 2 at higher drive levels and will be highly deficient in such regimes. For example, the permeability  $\mu$  is not only nonconstant for the data, but is in fact a multivalued map depending on both  $H$  and  $\sigma$ . As detailed in [2, 3], the assumption of a constant Young's modulus  $E^H$  and corresponding compliance  $s^H$  is also invalid for large field fluctuations, and a variable Young's modulus  $E(H, \sigma)$  and compliance  $s(H, \sigma)$  must be employed to attain accurate models.

There are numerous approaches for extending the magnetomechanical term  $d_{33} H$  in (1a) to include the nonlinear dynamics and hysteresis observed at moderate to high drive levels. However, most previous investigations have focussed on specific magnetic or magnetostrictive components of the system and few results are currently available which address the coupled magnetoelastic properties of magnetostrictive materials. For the magnetic regime, modeling techniques include micromechanical characterizations [4], phenomenological and Preisach approaches [5, 6, 7], the inclusion of specific nonlinear effects [8, 9], and domain theory based upon mean field equilibrium thermodynamics [10, 11, 12]. The modeling of strain effects due to the magnetostriction has received less attention and is less developed than the theory for magnetization. Current magnetostriction models are typically based upon either energy-based theories which quantify the interaction between atomic moments in a crystal lattice [13, 14, 15, 16] or polynomial expansions constructed to quantify the phenomenological behavior of the magnetostriction [17, 18]. With suitable assumptions, both approaches yield models in which the magnetostriction is characterized in terms of even powers of the magnetization (such a relation can be observed in the experimental data of Figure 2). To extend (1a) to a nonlinear model which characterizes strains in terms of input fields, it is necessary to quantify the coupled magnetic, magnetostrictive, and elastic properties of the material. Certain aspects of this problem are considered in [16, 19, 20] for magnetostrictive materials and [21] for electrostrictives. Models and corresponding numerical methods appropriate for quantifying strains generated by magnetostrictive transducers in general control applications are still lacking, however, and it is this problem which we address here.

To model the relationship between the input current  $I(t)$  and output strains  $e(t)$ , we consider the magnetic, magnetostrictive and elastic components in the system. To model the first, the Jiles-Atherton mean field theory for ferromagnetic hysteresis is modified to provide an energy-based relationship between the current  $I(t)$  applied to the solenoid and the resulting magnetization  $M(t)$ .

A quadratic moment rotation model then yields the output magnetostriction  $\lambda(t)$ . This provides a nonlinear and hysteretic analogue to the linear term  $d_{33}H$  in (1a). As demonstrated in [22], the magnetostriction provides adequate fits to experimental strain data at low to moderate drive levels. At high input levels, however, it is inadequate since it incorporates only active contributions to the strain and neglects material or passive strain effects. To model these effects, force balancing is used to derive a dynamic PDE model quantifying the rod dynamics. This PDE model has the form of a wave equation with magnetostrictive inputs and boundary conditions which model the prestress mechanism and mechanical return. The solution to this system provides the rod displacements and corresponding total strains. A comparison between the strain relations employed in this model and the linear relation (1a) is provided in Section 4.

Due to the generality of the PDE model, it is not possible to obtain an analytic solution specifying the rod displacements. To address this issue, we present in Section 5 appropriate numerical methods for approximating the spatial and temporal components of the PDE model. We consider a Galerkin finite element discretization in space which reduces the PDE to a matrix ODE system which evolves in time. The dynamics of the ODE system are approximated through a finite difference discretization to obtain a discrete time system having the measured current to the solenoid as input. The validity of the model and approximation method are illustrated in Section 6 through comparison with experimental data. It is demonstrated that the model characterizes the inherent magnetic hysteresis and accurately quantifies the strains and displacements output by the transducer.

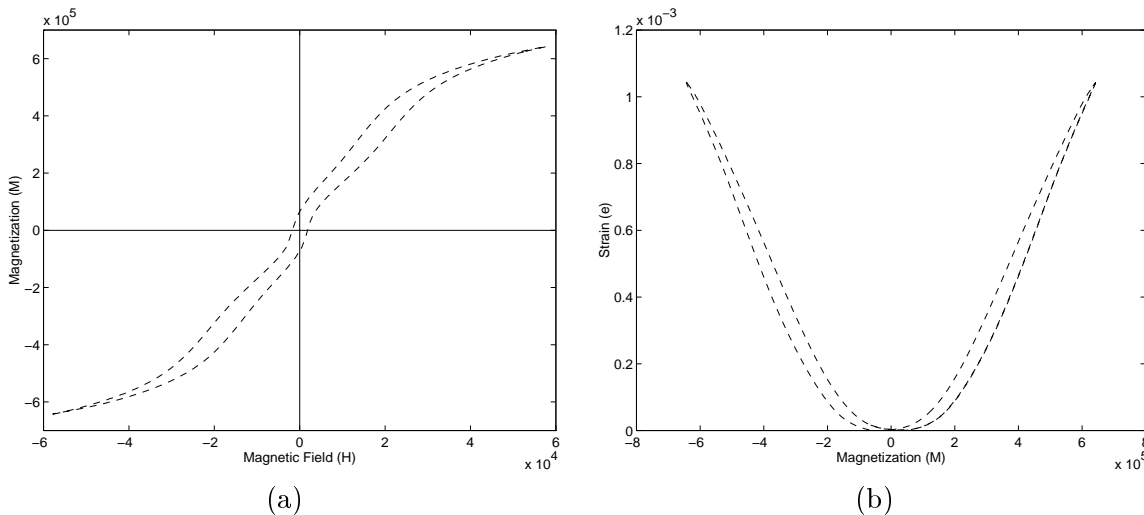


**Figure 2.** Relationship in experimental data between (a) the magnetic field  $H$  and the magnetization  $M$ , and (b) the magnetization  $M$  and the generated strains  $e$ .

## 2 Magnetization and Magnetostriction Models

The magnetization and magnetostriction models which we employ are based upon domain and domain wall theory for ferromagnetic materials. In ferromagnetic materials such as Terfenol-D, moments are highly aligned in regions termed domains at temperatures below the Curie point. The transition regions between domains are termed domain walls. Magnetization in such materials can then be described through quantification of domain configurations while magnetostriction can be characterized through the determination of the deformations which occur when moment configurations change.

## 2.1 Magnetization Model

The model which is employed for the magnetic component of the system is based upon the thermodynamic mean field theory of Jiles and Atherton [10, 11, 12]. In this approach, hysteresis-free (anhysteretic), irreversible and reversible components of the magnetization are quantified and used to characterize the total magnetization generated by an input magnetic field. The anhysteretic magnetization  $M_{an}$  is attributed to moment rotation within domains and is completely reversible. Such magnetization curves are rarely observed in laboratory materials, however, due to the presence of defects or second-phase materials (e.g., Dysprosium in Terfenol-D) which provide minimum energy states that impede domain wall movement and subsequent bulk moment reorientation. These inclusions or defects are often referred to as pinning sites. The effects of pinning on domain wall movement is quantified through the theory of Jiles and Atherton through consideration of reversible  $M_{rev}$  and irreversible  $M_{irr}$  components of the magnetization. For low field variations about an equilibrium level, the magnetization is reversible since the domain walls bulge but remain pinned at the inclusions. At higher input levels, the walls attain sufficient energy to break the pinning sites (move out of the minimum energy state) and intersect remote pinning sites. This leads to an irreversible change in magnetization and provides a significant mechanism for hysteresis. The reader is referred to [10, 13, 23] for additional details and discussion of other experimental phenomena, such as Barkhausen discontinuities, which are attributed to domain wall effects. This approach was initially employed in [22, 24, 25] to model magnetostrictive transducers. We summarize here pertinent details and indicate extensions from the original model.

To quantify  $M_{an}$ ,  $M_{rev}$  and  $M_{irr}$ , it is necessary to first determine the effective field  $H_{eff}$  which acts upon magnetic moments in the Terfenol rod. As detailed in [10, 11],  $H_{eff}$  is dependent upon the magnetic field generated by the solenoid, magnetic moment interactions, crystal and stress anisotropies, temperature and the transducer architecture (e.g., end effects). In [10, 22], it is illustrated that for large prestresses, stress anisotropies dominate crystalline anisotropies; hence for this model, crystalline anisotropies are neglected. Under the assumption of fixed temperature and quasi-static operating conditions, the effective field is then modeled by

$$H_{eff}(t, x) = H(t, x) + \alpha M(t, x) + H_\sigma(t, x)$$

where  $x$  denotes the longitudinal coordinate. Here  $H$  is the field generated by a solenoid with  $n$  turns per unit length,  $\alpha M$  quantifies the field due to magnetic interactions between moments, and  $H_\sigma$  is the field due to magnetoelastic domain interactions. The parameter  $\alpha$  quantifies the amount of domain interaction. For the prestress mechanism under consideration, it is demonstrated in [22] that the approximation  $H_\sigma = \frac{9}{2} \frac{\lambda_s \sigma_0}{\mu_0 M_s^2} M$  provides an adequate average of the stress contributions to the effective field. Here  $\lambda_s$  and  $M_s$  respectively denote the saturation magnetostriction and magnetization while  $\mu_0$  is the free space permeability. The magnetic interactions and stress coefficient can then be combined into the single coefficient  $\tilde{\alpha} = \alpha + \frac{9}{2} \frac{\lambda_s \sigma_0}{\mu_0 M_s^2}$  which must be experimentally determined for a given system.

Empirical studies have indicated that under a variety of operating conditions, a reasonable approximation to the effective field is provided by

$$H_{eff}(t, x) = nI(t)\varphi(x) + \tilde{\alpha}M(t, x) \quad (2)$$

where  $I(t)$  is the current to the solenoid and  $\varphi(x)$  is an empirically-determined function which incorporates transducer anomalies, such as end effects, that produce nonuniform field characteristics along the length of the rod. It should be noted that while the expression (2) is time-dependent, it must be restricted to low frequencies since the present model does not incorporate AC losses. The extension of this model to incorporate eddy current losses is under investigation.

For a computed effective field  $H_{eff}$ , Boltzmann statistics are used to quantify the anhysteretic magnetization in terms of the Langevin function

$$M_{an}(t, x) = M_s \left[ \coth \left( \frac{H_{eff}(t, x)}{a} \right) - \frac{a}{H_{eff}(t, x)} \right]. \quad (3)$$

The constant  $a = \frac{\mathcal{N}k_B T}{\mu_0 M_s}$ , where  $k_B$  is Boltzmann's constant,  $\mathcal{N}$  denotes the domain density and  $k_B T$  represents the Boltzmann thermal energy, is treated as a parameter to be identified since  $\mathcal{N}$  is unknown.

As detailed in [10, 11], quantification of the energy required to break pinning sites yields the expression

$$\frac{\partial M_{irr}}{\partial t}(t, x) = \frac{dI}{dt} \varphi(x) \cdot \frac{M_{an}(t, x) - M_{irr}(t, x)}{k\delta - \tilde{\alpha} [M_{an}(t, x) - M_{irr}(t, x)] \frac{dM_{irr}}{dM}} \quad (4)$$

for the time rate of change of the irreversible magnetization curve. The constant  $k$  has the form  $k = \frac{\langle p \rangle \langle \varepsilon_\pi \rangle}{2m\mu_0(1-c)}$ , where  $\langle p \rangle$  is the average density of pinning sites,  $\langle \varepsilon_\pi \rangle$  is the average energy for  $180^\circ$  walls,  $c$  is a reversibility coefficient, and  $m$  is the magnetic moment per unit volume of a typical domain. The parameter  $k$  provides a measure of the average energy required to break pinning sites and is also treated as a parameter to be estimated since  $\langle p \rangle$ ,  $c$  and  $\langle \varepsilon_\pi \rangle$  are unknown. The parameter  $\delta$  is defined to have the value  $+1$  when  $\frac{dH}{dt} > 0$  and  $-1$  when  $\frac{dH}{dt} < 0$  to guarantee that pinning always opposes changes in magnetization.

The reversible magnetization quantifies the degree to which domain walls bulge before attaining the energy necessary to break the pinning sites. To a first approximation, the reversible magnetization is given by

$$M_{rev}(t, x) = c[M_{an}(t, x) - M_{irr}(t, x)] \quad (5)$$

(see [11]). The reversibility coefficient  $c$  can be estimated from the ratio of the initial and anhysteretic differential susceptibilities [12] or through a least squares fit to data.

The total magnetization is then given by

$$M(t, x) = M_{rev}(t, x) + M_{irr}(t, x) \quad (6)$$

where  $M_{irr}$  and  $M_{rev}$  are defined in (4) and (5) and the anhysteretic magnetization is given by (3). For implementation purposes, it is necessary to numerically integrate the expression (4) to obtain  $M_{irr}$ . For the results in Section 4, this was accomplished via Euler's method. If higher accuracy is required, methods such as a trapezoid rule or Runge-Kutta method can be employed.

## 2.2 Magnetostriction Model

The second magnetomechanical component to be modeled is the deformations which occur when moment configurations are altered by an applied field  $H$ . These deformations are typically quantified through either an energy formulation [13, 14, 15, 16] or a phenomenological series expansion involving even powers of the magnetization [17, 18].

In the first case, general relations quantifying the material deformations are obtained through the minimization of various energy functionals. For example, one choice is the total energy expression

$$E = E_{mag} + E_{el} + E_{anis} \quad (7)$$

where the magnetoelastic energy  $E_{mag}$  quantifies the interactions between atomic magnetic moments in a crystal lattice,  $E_{el}$  denotes the elastic energy, and  $E_{anis}$  is the crystal anisotropy energy. As detailed in [13, 15], minimization of (7) yields a general expression for the anisotropic magnetostriction.

The situation is simplified in the regime considered here since the magnetic moments are essentially perpendicular to the applied field due to the manner of rod solidification and the compression provided by the prestress mechanism. In this case, energy minimization yields the isotropic single-valued relation

$$\lambda(t, x) = \frac{3}{2} \frac{\lambda_s}{M_s^2} M^2(t, x) \quad (8)$$

between the magnetization  $M$  and magnetostriction  $\lambda$ .

A second approach for modeling the magnetostriction is to employ the symmetry about  $M = 0$  to formulate a series expansion

$$\lambda(t, x) = \sum_{i=0}^{\infty} \gamma_i M^{2i}(t, x) \quad (9)$$

which empirically relates the magnetization and magnetostriction [17, 18]. The series is typically truncated after  $i = 1$  or  $i = 2$  to obtain a model which can be efficiently implemented. Note that the constant term yields elastic strains while  $i = 1$  yields the quadratic term obtained in (8) through an energy formulation.

The use of the quadratic expression (8) or a truncation of (9) in a transducer model requires the identification of the physical constants  $M_s, \lambda_s$  or the empirical constants  $\gamma_0, \gamma_1, \dots, \gamma_N$ . As will be observed in the experimental results of Section 5, the saturation magnetization  $M_s$  varies little between samples of Terfenol-D, and values identified for the transducer are very close to published material specifications. The saturation magnetostriction  $\lambda_s$  exhibits more dependence on operating conditions due to its dependence on the initial orientation of moments; hence it must be estimated for each transducer configuration. For the remainder of this discussion, the quadratic magnetostriction model (8) is employed.

### 3 Strain Model for the Terfenol Rod

The expression (8) quantifies the magnetostriction which occurs when moments within the material reorient in response to an applied field. This provides a generalization of the term  $d_{33}H$  in (1a) to accommodate the nonlinear dynamics inherent to the material at moderate to high drive levels. It ignores, however, the elastic properties of the material which are quantified in (1a) by the term  $s^H \sigma$ . In this section, we build on prior work to address this issue through consideration of a PDE model for the Terfenol rod which employs the field-induced magnetostriction  $\lambda(t, x)$  as input. This provides a partially coupled model which incorporates both structural dynamics and magnetic hysteresis.

For modeling purposes, we consider the Terfenol rod, prestress mechanism and end mass from the transducer depicted in Figure 1. The rod is assumed to have length  $L$ , cross-sectional area  $A$  and longitudinal coordinate  $x$ . The density, Young's modulus and internal damping coefficient are denoted by  $\rho, E$  and  $c_D$ , respectively. The left end of the rod ( $x = 0$ ) is assumed fixed while the right end is constrained by the spring washer which is modeled by a linear translational spring having stiffness  $k_L$  and damping coefficient  $c_L$ . It is noted that due to the compression bolt and spring washers, the rod is subjected to a prestress  $\sigma_0$ . Finally, the attached end mass is modeled by a point mass  $M_L$ .

The displacements of the rod at a point  $x$  and time  $t$  can be specified relative to either the unstressed state or the equilibrium state attained by the material after a prestress  $\sigma_0$  is applied. The longitudinal displacements relative to the unstressed and prestressed equilibrium states are denoted by  $\bar{u}(t, x)$  and  $u(t, x)$ , respectively. To relate the two, it is noted that when the prestress  $\sigma_0$  is applied,

the free end of the rod displaces by an amount

$$\bar{u}_0 = \frac{L}{E} \sigma_0$$

as illustrated in Figure 3. Under the assumption of homogeneous material properties and a uniform cross-sectional area, this produces a displacement

$$\bar{u}_0(x) = \bar{u}_0 \frac{x}{L}$$

for  $0 \leq x \leq L$ . The time-dependent displacements relative to the unstressed and prestressed equilibrium states are then related by the equation

$$u(t, x) = \bar{u}(t, x) - \bar{u}_0(x). \quad (10)$$

Note that for a compressive prestress  $\sigma_0$ ,  $\bar{u}_0$  and hence  $\bar{u}_0(x)$  will be negative.

We consider first a dynamic model in terms of the displacement at  $\bar{u}(t, x)$ . Under the assumptions of linear elasticity, small displacements, and Kelvin-Voigt damping, the stress at a point  $x$ ,  $0 < x < L$ , is given by

$$\bar{\sigma}(t, x) = E \frac{\partial \bar{u}}{\partial x}(t, x) + c_D \frac{\partial^2 \bar{u}}{\partial x \partial t}(t, x) - E \lambda(t, x) \quad (11)$$

where  $\lambda$  is given by (8). When integrated across the rod, this yields the inplane resultant

$$\bar{N}_{Tot}(t, x) = EA \frac{\partial \bar{u}}{\partial x}(t, x) + c_D A \frac{\partial^2 \bar{u}}{\partial x \partial t}(t, x) - EA \lambda(t, x). \quad (12)$$

Force balancing then yields the wave equation

$$\rho A \frac{\partial^2 \bar{u}}{\partial t^2} = \frac{\partial \bar{N}_{Tot}}{\partial x}$$

as a model for the internal rod dynamics.

To obtain appropriate boundary conditions, it is first noted that the fixed end of the rod satisfies the condition  $\bar{u}(t, x) = 0$ . At the end  $x = L$ , we consider an infinitesimal section having the orientation depicted in Figure 4. Force balancing then yields the boundary condition

$$\bar{N}_{tot}(t, L) + k_L [\bar{u}(t, L) - \bar{u}_0] + c_L \frac{\partial \bar{u}}{\partial t}(t, L) + \sigma_0 A = -M_L \frac{\partial^2 \bar{u}}{\partial t^2}(t, L) \quad (13)$$

(a more general discussion regarding the derivation of general elastic boundary conditions can be found in [26]). Note that when  $\bar{u}(t, L) = \bar{u}_0$  and  $\frac{\partial \bar{u}}{\partial t} = \frac{\partial^2 \bar{u}}{\partial t^2} = 0$ , the boundary condition (13) reduces

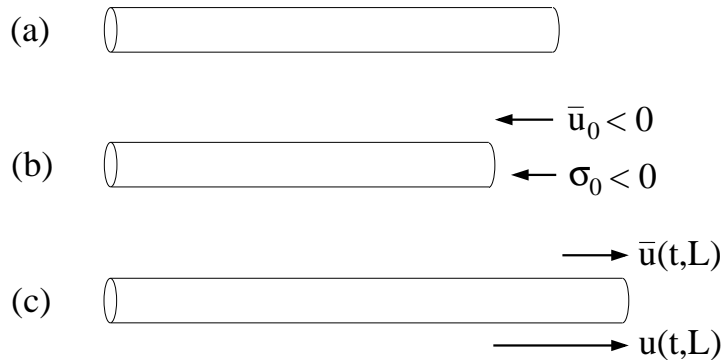


**Figure 3.** (a) Unstressed rod, (b) End displacement  $\bar{u}_0 = L\sigma_0/E$  due to a prestress  $\sigma_0$ , and (c) Time-dependent end displacements  $\bar{u}(t, L)$  and  $u(t, L) = \bar{u}(t, L) - \bar{u}_0$ .



to the equilibrium condition

$$\bar{N}_{tot}(t, L) = -\sigma_0 A.$$

When combined with initial conditions, the strong form of the model is then

$$\begin{aligned} \rho A \frac{\partial^2 \bar{u}}{\partial t^2} &= \frac{\partial \bar{N}_{tot}}{\partial x} \\ \left\{ \begin{array}{l} \bar{u}(t, 0) = 0 \\ \bar{N}_{tot}(t, L) = -k_L [\bar{u}(t, L) - \bar{u}_0] - c_L \frac{\partial \bar{u}}{\partial t}(t, L) - M_L \frac{\partial^2 \bar{u}}{\partial t^2}(t, L) - \sigma_0 A \end{array} \right. & \quad (14) \\ \left\{ \begin{array}{l} \bar{u}(0, x) = \bar{u}_0(x) \\ \frac{\partial \bar{u}}{\partial t}(0, x) = 0. \end{array} \right. \end{aligned}$$

It is noted that the initial conditions incorporate the equilibrium displacement  $\bar{u}_0(x)$  due to the prestress  $\sigma_0$ .

To define a weak or variational form of the model, the state  $\bar{u}$  is considered in the state space  $X = L^2(0, L)$  and the space of test functions is taken to be  $V = H_L^1(0, L) \equiv \{\phi \in H^1(0, L) \mid \phi(0) = 0\}$ . Multiplication by test functions followed by integration then yields the weak form

$$\begin{aligned} \int_0^L \rho A \frac{\partial^2 \bar{u}}{\partial t^2} \phi \, dx &= - \int_0^L \left[ EA \frac{\partial \bar{u}}{\partial x} + c_D A \frac{\partial^2 \bar{u}}{\partial x \partial t} - EA \lambda + \sigma_0 A \right] \frac{\partial \phi}{\partial x} \, dx \\ &\quad - \left[ k_L [\bar{u}(t, L) - \bar{u}_0] + c_L \frac{\partial \bar{u}}{\partial t}(t, L) + M_L \frac{\partial^2 \bar{u}}{\partial t^2}(t, L) \right] \phi(L) \end{aligned} \quad (15)$$

for all  $\phi \in V$ . The consideration of the prestress as a distributed input rather than a boundary condition follows from integration by parts. This formulation illustrates that if the prestress is negated by a constant input magnetostriction  $\lambda = \sigma_0/E$ , the system has the equilibrium solution  $\bar{u}(t, x) = 0$ . Conversely, the retention of the prestress as a boundary condition illustrates that in the absence of an applied current and resulting magnetostriction, the system will have the solution  $\bar{u}(t, x) = \bar{u}_0(x)$  and hence retain the initial offset for all time.

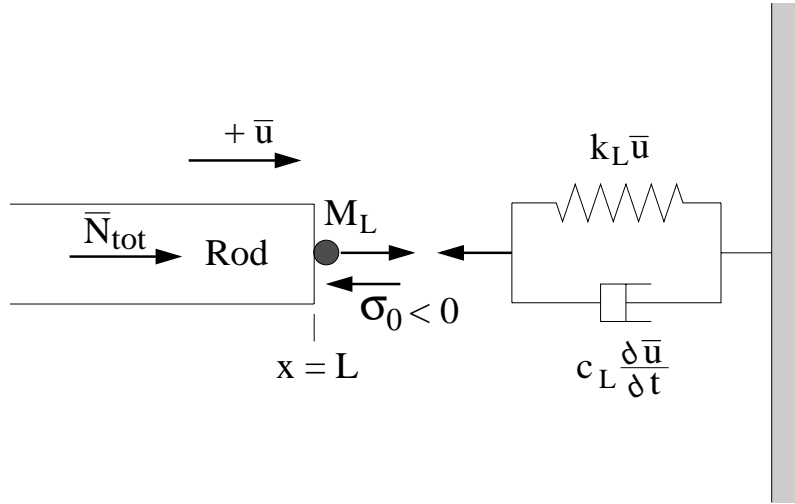


**Figure 4.** Orientation of spring forces, edge reactions and resultants for the Terfenol rod.

For many applications, the offset  $\bar{u}_0(x)$  due to the prestress  $\sigma_0$  is not consistent with strain or displacement data measured from the equilibrium prestressed state. For such cases, it is advantageous to consider the system satisfied by the perturbed displacement  $u(t, x)$ . Substitution of the expression (10) into (11) yields the stress relation

$$\sigma(t, x) = E \frac{\partial u}{\partial x}(t, x) + c_D \frac{\partial^2 u}{\partial x \partial t} - E \lambda(t, x) + \sigma_0 \quad (16)$$

while substitution into (12) and (13) yields the strong form of the model

$$\begin{aligned} \rho A \frac{\partial^2 u}{\partial t^2} &= \frac{\partial N_{tot}}{\partial x} \\ \begin{cases} u(t, 0) = 0 \\ N_{tot}(t, L) = -k_L u(t, L) - c_L \frac{\partial u}{\partial t}(t, L) - M_L \frac{\partial^2 u}{\partial t^2}(t, L) \end{cases} \\ \begin{cases} u(0, x) = 0 \\ \frac{\partial u}{\partial t}(0, x) = 0. \end{cases} \end{aligned} \quad (17)$$

The initial displacement in this case is  $u(x, 0) = 0$  since  $u$  denotes displacements from the prestressed equilibrium state.

The corresponding weak form of the model is

$$\begin{aligned} \int_0^L \rho A \frac{\partial^2 u}{\partial t^2} \phi \, dx &= - \int_0^L \left[ EA \frac{\partial u}{\partial x} + c_D A \frac{\partial^2 u}{\partial x \partial t} - EA \lambda \right] \frac{\partial \phi}{\partial x} \, dx \\ &\quad - \left[ k_L u(t, L) + c_L \frac{\partial u}{\partial t}(t, L) + M_L \frac{\partial^2 u}{\partial t^2}(t, L) \right] \phi(L) \end{aligned} \quad (18)$$

for all  $\phi \in V$ . The solution  $u(t, x)$  to (17) or (18) provides the longitudinal displacements of the rod from the perturbed state  $\bar{u}_0(x)$  produced by the prestress  $\sigma_0$ . In the absence of an applied input  $\lambda(t, x)$ , the system (18) will have the equilibrium solution  $u(t, x) \equiv 0$  as compared with the offset solution  $\bar{u}(t, x) = \bar{u}_0(x)$  which satisfies (15). Hence the model (18) and corresponding stress relation (16) are preferable when data is measured relative to the prestressed state. This structural model is summarized along with the previously-defined magnetization and magnetostriction models in Table 1. Note that in the weak form (18), displacements and test functions are differentiated only once compared with the second derivatives required in the strong form. This reduces the smoothness requirements on the finite element basis when constructing an approximation method.

Magnetization Model	$H(t, x) = nI(t)\varphi(x)$ $H_{eff}(t, x) = H(t, x) + \tilde{\alpha}M(t, x)$ $M_{an}(t, x) = M_s \left[ \coth \left( \frac{H_{eff}(t, x)}{a} \right) - \left( \frac{a}{H_{eff}(t, x)} \right) \right]$ $\frac{\partial M_{irr}}{\partial t}(t, x) = n \frac{dI}{dt} \varphi(x) \cdot \frac{M_{an}(t, x) - M_{irr}(t, x)}{k\delta - \tilde{\alpha}[M_{an}(t, x) - M_{irr}(t, x)] \frac{dM_{irr}}{dM}}$ $M_{rev}(t, x) = c[M_{an}(t, x) - M_{irr}(t, x)]$ $M(t, x) = M_{rev}(t, x) + M_{irr}(t, x)$
Magnetostriction Model	$\lambda(t, x) = \frac{3}{2} \frac{\lambda_s}{M_s^2} M^2(t, x)$
Structural Dynamics of Terfenol rod	$\int_0^L \rho A \frac{\partial^2 u}{\partial t^2} \phi dx = - \int_0^L \left[ EA \frac{\partial u}{\partial x} + c_D A \frac{\partial^2 u}{\partial x \partial t} - EA \lambda \right] \frac{\partial \phi}{\partial x} dx$ $- \left[ k_L u(t, L) + c_L \frac{\partial u}{\partial t}(t, L) + M_L \frac{\partial^2 u}{\partial t^2}(t, L) \right] \phi(L)$

**Table 1.** Time-dependent model quantifying the magnetization  $M(t, x)$ , the output magnetostriction  $\lambda(t, x)$  and rod displacements  $u(t, x)$ .

## 4 Comparison with the Linear Model

The stress relation (16) generalizes the linear constitutive law (1a) to include both Kelvin-Voigt damping and hysteretic and nonlinear magnetomechanical inputs. To verify this, it is noted that in this regime,  $s^H = 1/E$  and  $e = \frac{\partial u}{\partial x}$  so that (16) can be reformulated as

$$e = s^H (\sigma - \sigma_0) + \lambda - \frac{c_D}{E} \dot{e}.$$

To illustrate that  $\lambda$  provides the active strain contributions modeled by  $d_{33}H$  in the linear model (1a), we take  $c_D = \sigma_0 = 0$  and employ the relation (8) to obtain

$$e = s^H \sigma + \frac{3}{2} \frac{\lambda_s}{M_s^2} M^2.$$

Linearization about a biasing magnetization level  $M_0$  then yields the strain expression

$$e = s^H \sigma + \frac{3}{2} \frac{\lambda_s}{M_s^2} (2MM_0 - M_0^2). \quad (19)$$

To express the magnetization and resulting strain in terms of the applied magnetic field, it is noted that in the absence of hysteresis, the magnetization satisfies the anhysteretic relation

$$\begin{aligned} M &= M_s \left[ \coth \left( \frac{H_{eff}}{a} \right) - \frac{a}{H_{eff}} \right] \\ &= M_s \left( \frac{H_{eff}}{3a} \right) + \mathcal{O} \left( \frac{H_{eff}^3}{a^3} \right). \end{aligned}$$

To linearize, the high order terms in the Taylor expansion are neglected to obtain

$$M = \frac{M_s}{3a}(H + \tilde{\alpha}M)$$

which implies that

$$M = \frac{M_s}{3a - M_s \tilde{\alpha}} H.$$

Hence (19) can be written as

$$e = s^H \sigma + \frac{3}{2} \frac{\lambda_s}{M_s^2} \left( \frac{M_s}{3a - M_s \tilde{\alpha}} \right)^2 (2HH_0 - H_0^2) \quad (20)$$

where  $H_0$  is the magnetic field required to produce the bias magnetization  $M_0$ .

As depicted in Figure 5, the total strain  $e$  is composed of a bias  $e_0$  due to the biasing magnetization  $M_0$  and bidirectional strains  $\Delta e$  about  $e_0$ . To specify  $e_0$  and  $\Delta e$ , we reformulate (20) as

$$\begin{aligned} e &= \left[ s^H \sigma + \frac{3\lambda_s}{M_s^2} \left( \frac{M_s}{3a - M_s \tilde{\alpha}} \right)^2 H_0 (H - H_0) \right] + \frac{3}{2} \frac{\lambda_s}{M_s^2} \left( \frac{M_s}{3a - M_s \tilde{\alpha}} \right)^2 H_0 \\ &= \Delta e + e_0 \end{aligned}$$

where  $e_0 = \frac{3}{2} \frac{\lambda_s}{M_s^2} \left( \frac{M_s}{3a - M_s \tilde{\alpha}} \right)^2 H_0$  and

$$\Delta e = s^H \sigma + \frac{3\lambda_s}{M_s^2} \left( \frac{M_s}{3a - M_s \tilde{\alpha}} \right)^2 H_0 (H - H_0)$$

(Note that  $\Delta e = s^H \sigma$  when  $H = H_0$ ). With the definitions

$$\begin{aligned} d_{33} &= \frac{3\lambda_s}{M_s^2} \left( \frac{M_s}{3a - M_s \tilde{\alpha}} \right)^2 H_0 \\ \Delta H &= H - H_0, \end{aligned}$$

the bidirectional strains are then given by

$$\Delta e = s^H \sigma + d_{33} \Delta H$$

which is equivalent to the original linear expression (1a) when it is used to model bidirectional strains about a preset magnetization level  $M_0$ .

We conclude this section by noting that the reader can find further details regarding the decomposition of strains into passive components due to elastic properties of the material and nonlinear active components due to magnetostriction in [19, p. 180].

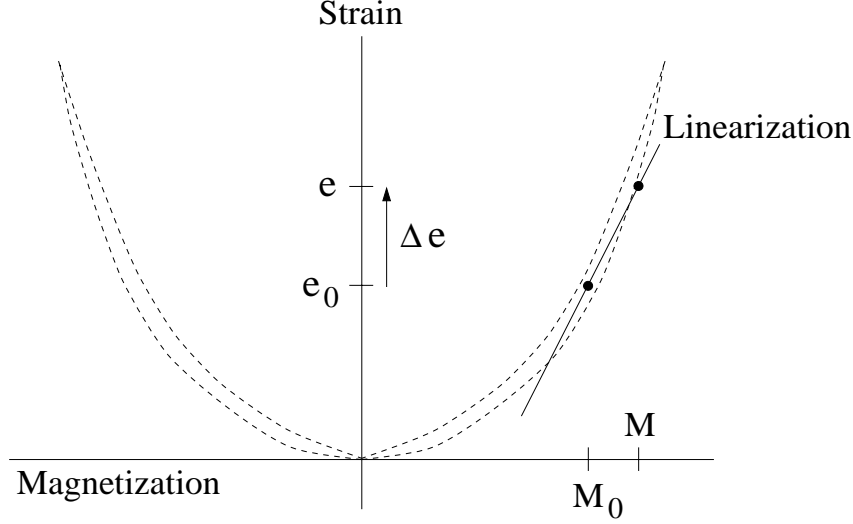


**Figure 5.** Linearization about the biasing magnetization  $M_0$  and the resulting bias strain  $e_0$ , bidirectional strain  $\Delta e$ , and total strain  $e = e_0 + \Delta e$ .

## 5 Approximation Method

To approximate the solution of (18), we consider a Galerkin discretization in space followed by a finite-difference approximation of the resulting temporal system. To this end, we consider a uniform partition of the interval  $[0, L]$  with points  $x_i = ih, i = 0, 1, \dots, N$  and stepsize  $h = L/N$  where  $N$  denotes the number of subintervals. The spatial basis  $\{\phi_i\}_{i=1}^N$  is comprised of linear splines, or ‘hat functions,’ of the form

$$\phi_i(x) = \frac{1}{h} \begin{cases} (x - x_{i-1}), & x_{i-1} \leq x < x_i \\ (x_{i+1} - x), & x_i \leq x < x_{i+1} \\ 0, & \text{otherwise} \end{cases}, \quad i = 1, \dots, N-1$$

$$\phi_N(x) = \frac{1}{h} \begin{cases} (x - x_{N-1}), & x_{N-1} \leq x \leq x_N \\ 0, & \text{otherwise} \end{cases}$$

(see [27] for details). A general basis function  $\phi_i$  and final basis function  $\phi_N$  are plotted in Figure 6.

The solution  $u(t, x)$  to (18) is then approximated by the expansion

$$u^N(t, x) = \sum_{j=1}^N u_j(t) \phi_j(x),$$

in the subspace  $H^N = \text{span}\{\phi_i\}_{i=1}^N$ . It should be noted that through the construction of the basis functions, the approximate solution satisfies  $u^N(t, 0) = 0$  and allows arbitrary displacements at  $x = L$ .

A semi-discrete matrix system is obtained by considering the approximate solution  $u^N(t, x)$  in (18) with the basis functions employed as test functions (this is equivalent to projecting the system (18) onto the finite dimensional subspace  $H^N$ ). This yields the second-order time-dependent vector system

$$Q\ddot{\vec{u}}(t) + C\dot{\vec{u}}(t) + K\vec{u}(t) = \vec{f}(t) \quad (21)$$

where  $\vec{u}(t) = [u_1(t), \dots, u_N(t)]$ . The mass, stiffness and damping matrices have the components

$$\begin{aligned}
[Q]_{ij} &= \begin{cases} \int_0^L \rho A \phi_i \phi_j dx & , \quad i \neq n \text{ and } j \neq n \\ \int_0^L \rho A \phi_i \phi_j dx + M_L & , \quad i = n \text{ and } j = n \end{cases} \\
[K]_{ij} &= \begin{cases} \int_0^L EA \phi_i' \phi_j' dx & , \quad i \neq n \text{ and } j \neq n \\ \int_0^L EA \phi_i' \phi_j' dx + k_L & , \quad i = n \text{ and } j = n \end{cases} \\
[C]_{ij} &= \begin{cases} \int_0^L c_D A \phi_i' \phi_j' dx & , \quad i \neq n \text{ and } j \neq n \\ \int_0^L c_D A \phi_i' \phi_j' dx + c_L & , \quad i = n \text{ and } j = n \end{cases}
\end{aligned}$$

while the force vector is defined by

$$[\vec{f}(t)]_i = \int_0^L EA \lambda(t, x) \phi_i'(x) dx$$

(here ' denotes a spatial derivative). With the definitions  $\vec{y}(t) = [\vec{u}(t), \dot{\vec{u}}(t)]^T$ ,

$$W = \begin{bmatrix} 0 & I \\ -Q^{-1}K & -Q^{-1}C \end{bmatrix} , \quad \vec{F}(t) = \begin{bmatrix} 0 \\ -Q^{-1}\vec{f}(t) \end{bmatrix} ,$$

the second-order system (21) can be posed as the first-order system

$$\begin{aligned}
\dot{\vec{y}}(t) &= W \vec{y}(t) + \vec{F}(t) \\
\vec{y}(0) &= \vec{y}_0 ,
\end{aligned} \tag{22}$$

where the  $2N \times 1$  vector  $\vec{y}_0$  denotes the projection of the initial conditions into the approximating space.

The system (22) must be discretized in time to permit numerical or experimental implementation. The choice of approximation method is dictated by accuracy and stability requirements, storage capabilities, sample rates, et cetera. A trapezoidal method can be advantageous for experimental implementation since it is moderately accurate, is A-stable, and requires minimal storage when implemented as a single step method. For temporal stepsizes  $\Delta t$ , a standard trapezoidal discretization yields the iteration

$$\begin{aligned}
\vec{y}_{j+1} &= \mathcal{W} \vec{y}_j + \frac{1}{2} \mathcal{F} [\vec{F}(t_j) + \vec{F}(t_{j+1})] \\
\vec{y}_0 &= \vec{y}(0) ,
\end{aligned} \tag{23}$$

where  $t_j = j\Delta t$  and  $\vec{y}_j$  approximates  $\vec{y}(t_j)$ . The matrices

$$\mathcal{W} = \left[ I - \frac{\Delta t}{2} W \right]^{-1} \left[ I + \frac{\Delta t}{2} W \right] , \quad \mathcal{F} = \Delta t \left[ I - \frac{\Delta t}{2} W \right]^{-1}$$

need only be created once when numerically or experimentally implementing the method. This yields approximate solutions having  $\mathcal{O}(h^2, (\Delta t)^2)$  accuracy. For applications in which data at future times  $t_{j+1}$  is unavailable, the algorithm (23) can be replaced by the modified trapezoidal iteration

$$\begin{aligned}\vec{y}_{j+1} &= \mathcal{W}\vec{y}_j + \mathcal{F}\vec{F}(t_j) \\ \vec{y}_0 &= \vec{y}(0).\end{aligned}$$

While this decreases slightly the temporal accuracy, for large sample rates with correspondingly small stepsizes  $\Delta t$ , the accuracy is still commensurate with that of the data.

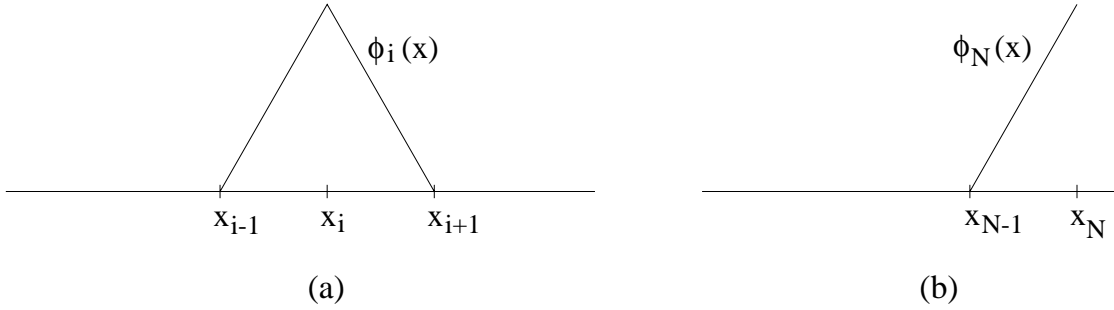


**Figure 6.** Linear basis functions (a)  $\phi_i(x)$  and (b)  $\phi_N(x)$ .

## 6 Experimental Validation

As summarized in Table 1, the magnetization model (6), magnetostriction model (8) and PDE (18) can be combined to yield time-dependent displacement values of the Terfenol rod for all points along its length in response to an input current  $I(t)$  to the solenoid. This model incorporates magnetic hysteresis, nonlinear strain properties and the coupling between the external strains generated by the material and the dynamics of the rod. In its present form, however, the model is not fully coupled since it does not yet incorporate the dynamic stress effects on the effective field and ensuing magnetization. This topic is under current investigation.

For the results which follow, experimental data was collected from a broadband transducer developed at Iowa State University (the general configuration of the transducer can be noted in Figure 1). A solid Terfenol-D ( $\text{Tb}_{0.3}\text{Dy}_{0.7}\text{Fe}_{1.9}$ ) rod having a length of 115 mm (4.53 in) and diameter of 12.7 mm (0.5 in) was employed in the transducer. Mechanical prestresses to the rod were generated by a variable prestress bolt at one end of the transducer and Belleville washers fitted at the opposite end of the rod. The results reported here were obtained with a prestress of  $\sigma_0 = 1.0$  ksi. Surrounding the rod were two coils consisting of an inner single layer 150-turn pickup coil and a multi-layer 900-turn drive coil. A current control amplifier (Techron 7780) provided the input to the drive coil to produce an applied AC magnetic field and DC bias as necessary. The reference signal to this amplifier was provided by a Tektronix spectrum analyzer and the applied magnetic field  $H$  generated by the drive coil had a frequency of 0.7 Hz and magnitude up to 70 kA/m.

A cylindrical permanent magnet surrounding the coils provided the capability for generating additional DC bias if necessary. This permanent magnet was constructed of Alnico V and was slit to reduce eddy current losses. Note that for the experiments reported here, biases generated in this manner were unnecessary and the permanent magnet was demagnetized to obtain unbiased data.

To determine a function  $\varphi(x)$  (see (2)) which characterizes transducer anomalies such as end effects, an axial Hall effect probe connected to a F.W. Bell Model 9500 gaussmeter was used to map the flux density and corresponding field along the length of the rod. The resulting function  $\varphi(x)$  is plotted in Figure 7 with the predominance of end effects readily noted.

The measured output from the transducer during operation included the current and voltage in the drive coil, the voltage induced in the pickup coil, and the rod displacement. The current  $I(t)$  was used to compute the field  $H(t, x) = nI(t)\varphi(x)$  applied to the rod. From the induced voltage in the pickup coil, the Faraday-Lenz law was used to compute the temporal derivative of the magnetic induction  $B$ . Integration then yielded the induction and magnetization  $M = \frac{1}{\mu_0}B - H$ . Both the field and magnetization were numerically filtered to remove the small biases due to instrumentation. A Lucas LVM-110 linear variable differential transformer, based upon changing reluctance, was used to measure the displacement of the rod tip. Corresponding strains at this point were then computed by dividing by the rod's length. The experimental data collected in this manner is plotted in Figures 8-10. Throughout the experiments, temperature was monitored using two thermocouples attached to the Terfenol-D sample and maintained within 5° C of the ambient temperature (23° C).

To employ the magnetization and structural model summarized in Table 1, appropriate parameters must be ascertained. These include the magnetization parameters  $\tilde{\alpha}, c, k, a, \lambda_s, M_s$ , the structural parameters  $\rho, E, c_D$ , the spring constants  $k_L, c_L$  and the end mass  $M_L$ . The values used here are summarized in Table 2. The magnetization parameters were estimated through a least squares fit to data as detailed in [22]. The values of  $\rho$  and  $E$  are published specifications for Terfenol-D while the damping parameters  $c_D$  and  $c_L$  were chosen within a range typical for the material. The spring stiffness coefficient  $k_L$  was measured through a compression test while the end mass  $M_L$  was measured directly. We note that while the specification of parameters in this manner provided adequate model fits, they are not optimal. To obtain optimal parameters and corresponding model fits, it is necessary to estimate all parameters through a least squares fit to data.

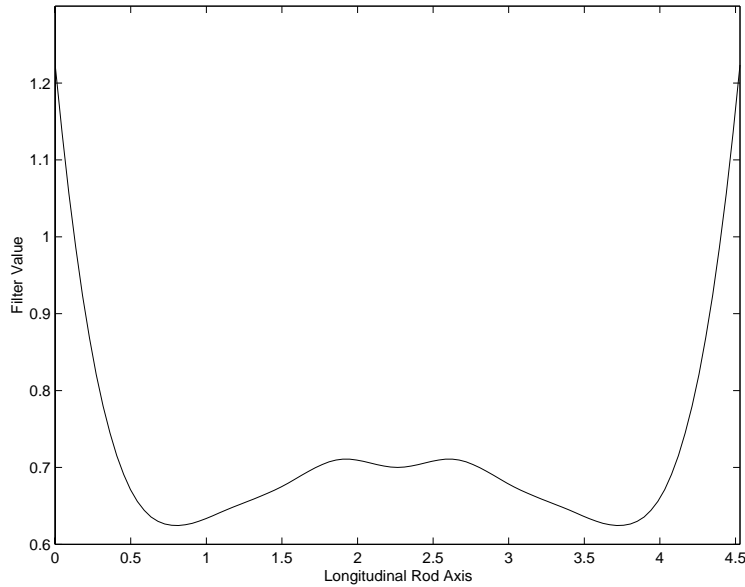


**Figure 7.** Empirical function  $\varphi(x)$  used to qualify transducer effects.



Magnetization Parameters	Structural Parameters	Spring and End Mass	Dimension
$M_s = 7.65 \times 10^5 \text{ A/m}$	$\rho = 9250 \text{ kg/m}^3$	$M_L = 0.5 \text{ kg}$	$L = 115 \text{ mm}$
$\lambda_s = 1005 \times 10^{-6}$	$E = 3 \times 10^{10} \text{ N/m}^2$	$k_L = 2 \times 10^6 \text{ N/m}$	$d = 12.7 \text{ mm}$
$a = 7012 \text{ A/m}$	$c_D = 3 \times 10^6 \text{ Ns/m}^2$	$c_L = 1 \times 10^3 \text{ Ns/m}$	
$k = 4000 \text{ A/m}$		$\sigma_0 = 1.0 \text{ ksi}$	
$\tilde{\alpha} = -0.01$			
$c = 0.18$			

**Table 2.** Physical parameters and dimensions employed in the magnetization and structural models.

### Magnetization Model

The domain wall model discussed in Section 3.1 and summarized in Table 1 provides a characterization of the magnetization  $M$  generated by an applied magnetic field  $H$ . The performance of the model under quasi-static (0.7 Hz) operating conditions is illustrated in Figure 8. It is observed that while the model accurately characterizes the measured magnetization over most of the range, certain aspects of the transducer behavior are not completely quantified at low field levels. The constricted behavior in the magnetization at low field levels has been observed by other researchers [23, 28] and is hypothesized to be due to  $180^\circ$  domain rotations. While quantification of this effect is ultimately desired, the accuracy and flexibility of the current magnetization model are sufficient for control applications in this operating regime.

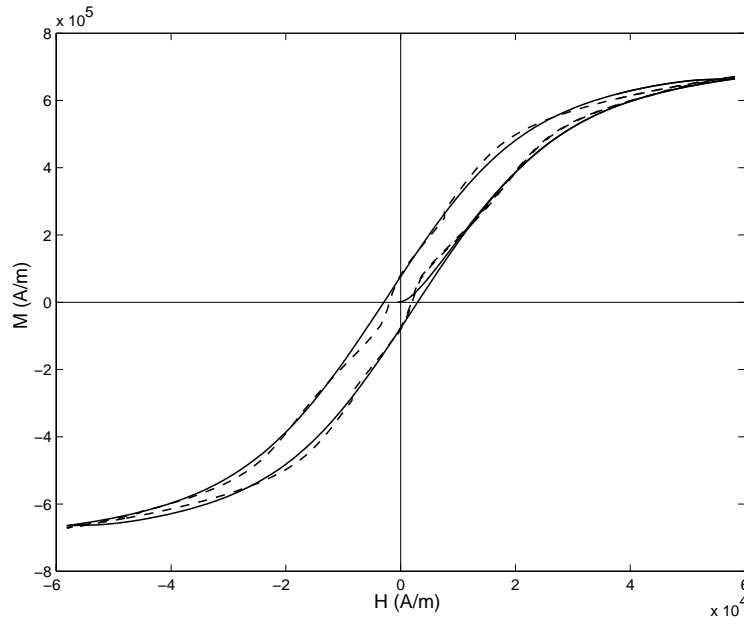


**Figure 8.** Experimental  $M$ - $H$  data (---) and model dynamics (—) at  $x=L$  with the magnetization  $M$  computed using filtered magnetic field data  $H(t, x) = nI(t)\varphi(x)$ ;

## Strain Model

The model summarized in Table 1 characterizes two aspects of the strain in the Terfenol rod. The magnetostriction  $\lambda$  quantifies the external or active component of the strain while  $e = \frac{\partial u}{\partial x}$  provides the total strain in the rod. The relationship between the two can be noted in the stress expressions (11) or (16). The total strain  $\frac{\partial u}{\partial x}$  incorporates both the elastic properties of the material and the magnetomechanical effects due to domain rotation; hence it is the quantity which models the strains measured in the transducer rod during experiments.

The modeled strain  $e(t, L) = \frac{u(t, L)}{L}$  at the rod tip is plotted with experimental data in Figures 9a and 10a. For comparison, the magnetostriction given by (8) is plotted with experimental data in Figures 9b and 10b. Recall that while the magnetic field, magnetization and strains are time-dependent, data was collected at a sufficiently low frequency (0.7 Hz) to avoid AC losses and harmonic effects. It is observed in Figure 9 that some discrepancy occurs in both the strain and magnetostriction due to limitations in the quadratic model (8). The total strain provided by the dynamic model does, however, include the hysteresis observed in the experimental data. This is a significant advantage over the modeled magnetostriction which is single-valued. This leads to the highly accurate model fit observed in Figure 10 where the relation between the input field  $H$  and the output strain  $e(t, L)$  at the rod tip is plotted.

For comparison purposes, we include in Figure 11 the corresponding model fits obtained when the filtering function  $\varphi(x)$  was omitted and an averaged field measurement was used to compute  $M$  and  $\lambda$ . This was the regime considered in [22] where it was demonstrated that use of magnetostriction rather than total strain led to an adequate model at low to moderate drive levels but provided inadequate fits at high input levels. These conclusions are reinforced by the model fits observed in Figure 11. It is noted that even when the saturation magnetostriction was scaled to the maximum experimentally observed value, the lack of hysteresis in the relation between  $M$  and  $\lambda$  led to an inadequate characterization of  $\lambda$  in terms of  $H$ . A comparison with Figures 9a and 10a again indicates the necessity of considering the total strains.

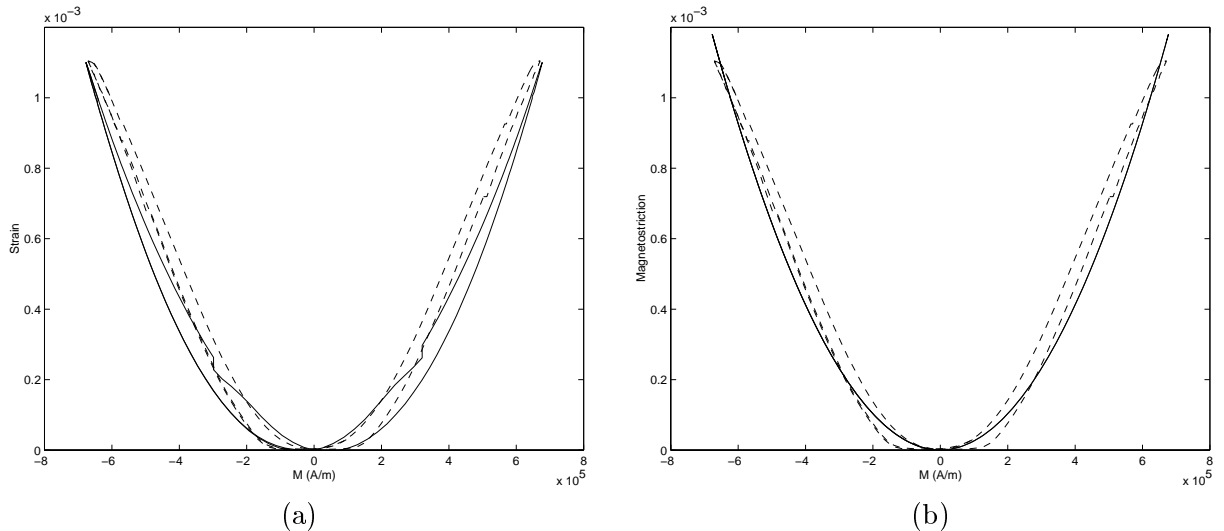


**Figure 9.** Experimental  $M$ -strain data (---) and model dynamics (—) with the magnetization  $M$  computed using filtered magnetic field data  $H(t, x) = nI(t)\varphi(x)$ ; (a) Total strain  $e(t, L)$ , (b) Magnetostriction  $\lambda(t, L)$ .

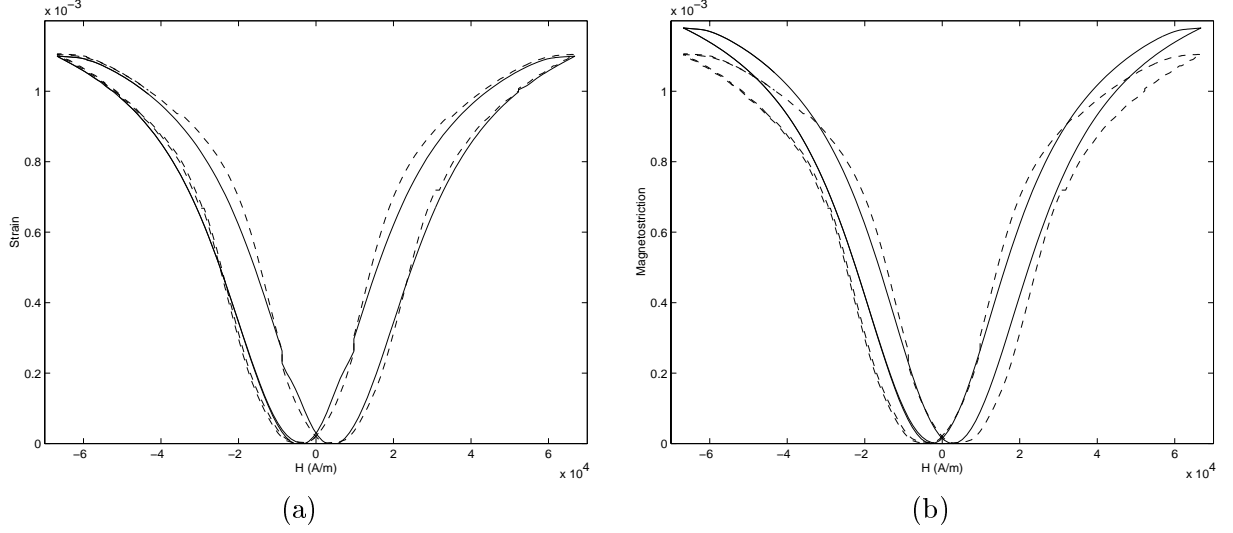


**Figure 10.** Experimental  $H$ -strain data (---) and model dynamics (—) computed using filtered magnetic field data  $H(t, x) = nI(t)\varphi(x)$ ; (a) Total strain  $e(t, L)$ , (b) Magnetostriction  $\lambda(t, L)$ .

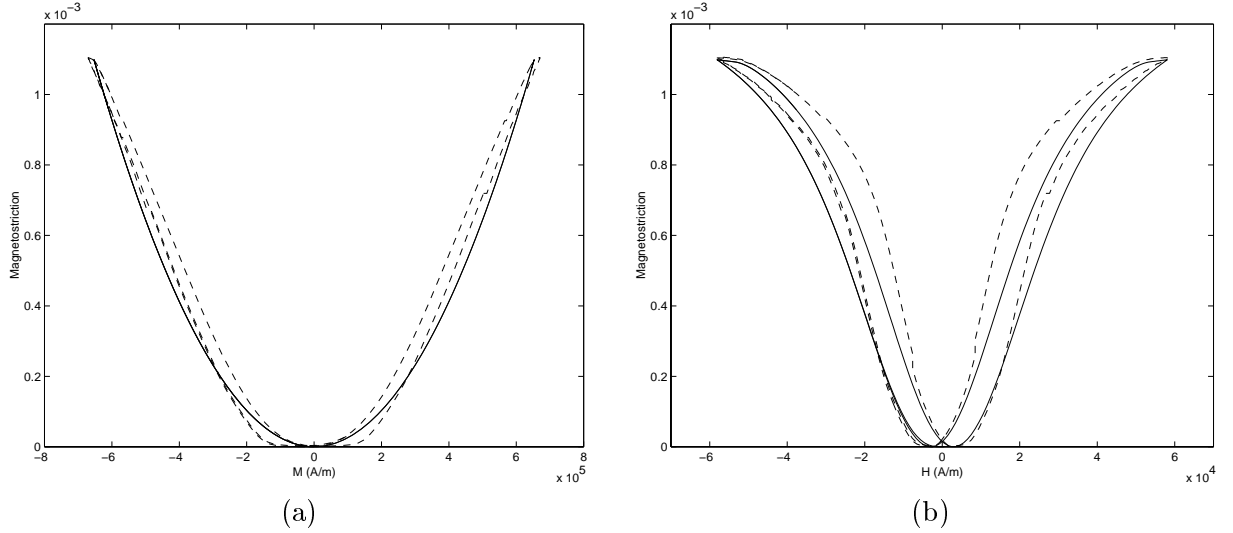


**Figure 11.** Experimental data strain (---) and model dynamics (—) computed using unfiltered magnetic field data  $H(t) = nI(t)$  and a scaled saturation magnetostriction  $\lambda_s$ ; (a)  $M$ - $\lambda$  relation, (b)  $H$ - $\lambda$  relation.

## 7 Concluding Remarks

This paper addresses the modeling of strains generated by magnetostrictive materials when employed in high performance transducers. The model extends the classical relation (1a), which includes elastic effects and a linear magnetomechanical component, to the regime in which magnetoelastic inputs are nonlinear and exhibit significant hysteresis. This is necessary to accommodate the dynamics

observed in current transducers at high drive levels and to provide a model for design and control applications in such regimes.

The model was constructed in three steps. In the first, the mean field theory of Jiles and Atherton was used to quantify the relation between the current input to the solenoid and the magnetization produced in the rod. This component of the model incorporates both inherent magnetic hysteresis and saturation effects at high field levels. In the second step, the magnetostriction due to the rotation of moments was quantified through consideration of a quadratic model posed in terms of the magnetization. When combined with the mean field magnetization model, this provided a means for extending the linear magnetoelastic relation (1a) to include the nonlinear dynamics and hysteresis observed at high field levels. Finally, force balancing provided a PDE model which quantified material displacements due to the magnetostriction. For a given input current, the solution to the PDE yields the displacements and strains produced by the rod.

While the PDE has the form of a wave equation, the nature of the boundary conditions modeling the prestress mechanism and end mass precluded analytic solution. Hence we approximated the solution through a finite element discretization in the spatial variable followed by a finite difference discretization in time. This yielded a vector system which could be iterated in time with the measured electric current or magnetic field data employed as input.

The examples illustrated that the resulting model yields the hysteresis observed in experimental strain data when plotted as function of the magnetization. This is a significant improvement over the magnetostriction which is modeled as a single-valued function of the magnetization. Finally, the accuracy of the model is reflected in the full relation between the input field  $H$  and strains  $e$  produced by the transducer.

## Acknowledgements

The authors express sincere appreciation to Tad Calkins and David Jiles for input regarding the modeling techniques employed here and to Brian Lund for his assistance in collecting the experimental data. The research of R.C.S. was supported in part by the Air Force Office of Scientific Research under the grant AFOSR F49620-95-1-0236. Financial support for M.J.D. and A.B.F. was provided by the NSF Young Investigator Award #CMS9457288 of the Division of Civil and Mechanical Systems.

## References

- [1] D.L. Hall and A.B. Flatau, "Nonlinearities, harmonics and trends in dynamic applications of Terfenol-D," Proceedings of the SPIE Conference on Smart Structures and Intelligent Materials, Vol. 1917, Part 2, 1993, pp. 929-939.
- [2] F.T. Calkins, M.J. Dapino and A.B. Flatau, "Effect of prestress on the dynamic performance of a Terfenol-D transducer," Proceedings of the SPIE, Smart Structures and Materials 1997: Smart Structures and Integrated Systems, San Diego, CA, March 1997, Vol. 3041, pp. 293-304.
- [3] M.J. Dapino, F.T. Calkins, A.B. Flatau and D.L. Hall, "Measured Terfenol-D material properties under varied applied magnetic field levels," Proceedings of the SPIE, Smart Structures and Materials 1996, San Diego, CA, March 1996, Vol. 2717-66.
- [4] W.F. Brown, *Magnetoelastic Interactions*, Springer-Verlag, Berlin, 1966.

- [5] J.B. Restorff, H.T. Savage, A.E. Clark and M. Wun-Fogle, "Preisach modeling of hysteresis in Terfenol-D," *J. Appl. Phys.*, 67(9), pp. 5016-5018, 1996.
- [6] A.A. Adly and I.D. Mayergoyz, "Magnetostriction simulation using anisotropic vector Preisach-type models," *IEEE Trans. Magn.*, 32(5), pp. 4773-4775, 1996.
- [7] R.C. Smith, "Hysteresis modeling in magnetostrictive materials via Preisach operators," *Journal of Mathematical Systems, Estimation and Control*, 8(2), summary pp. 249-252, 1998.
- [8] G.P. Carman and M. Mitrovic, "Nonlinear constitutive relations for magnetostrictive materials with applications to 1-D problems," *Journal of Intelligent materials Systems and Structures*, 6, pp. 673-684, 1995.
- [9] K.S. Kannan and A. Dasgupta, "Continuum magnetoelastic properties of Terfenol-D; what is available and what is needed," Adaptive Materials Symposium, Summer meeting of ASME-AMD-MD, UCLA, 1995.
- [10] D.C. Jiles, *Introduction to Magnetism and Magnetic Materials*, Chapman and Hall, New York, 1991.
- [11] D.C. Jiles and D.L. Atherton, "Theory of ferromagnetic hysteresis," *J. Magn. Magn. Mater.*, 61, pp. 48-60, 1986.
- [12] D.C. Jiles, J.B. Thoeke and M.K. Devine, "Numerical determination of hysteresis parameters for the modeling of magnetic properties using the theory of ferromagnetic hysteresis," *IEEE Trans. Magn.*, 28(1), pp. 27-35, 1992.
- [13] S. Chikazumi, *Physics of Ferromagnetism*, Second Edition, Oxford University Press, New York, 1997.
- [14] R. James and D. Kinderlehrer, "Theory of magnetostriction with applications to  $\text{Tb}_x\text{Dy}_{1-x}\text{Fe}_2$ ," *Philosophical Magazine B*, 68(2), pp. 237-74, 1993.
- [15] E.W. Lee, "Magnetostriction and magnetomechanical effects," *Reports on Prog. in Phys.*, 18, pp. 184-229, 1955.
- [16] M.J. Sablik and D.C. Jiles, "Coupled magnetoelastic theory of magnetic and magnetostrictive hysteresis," *IEEE Trans. Magn.*, 29(3), pp. 2113-2123, 1993.
- [17] D.C. Jiles, "Theory of the magnetomechanical effect," *Phys. D: Appl. Phys.*, 28, pp. 1537-1546, 1995.
- [18] M.J. Sablik, G.L. Burkhardt, H. Kwun and D.C. Jiles, "A model for the effect of stress on the low-frequency harmonic content of the magnetic induction in ferromagnetic materials," *J. Appl. Phys.*, 63(8), pp. 3930-3932, 1988.
- [19] E. du Trémolet de Lacheisserie, *Magnetostriction: Theory and Applications of Magnetoelasticity*, CRS Press, Ann Arbor, 1993.
- [20] L. Kvarnsjö, On characterization, modeling, and application of highly magnetostrictive materials," PhD dissertation, Royal Institute of Technology, TRITA-EEA-9301, ISSN 1100-1593, Stockholm, Sweden, 1993.

- [21] C.L. Hom and N. Shankar, "A dynamics model for nonlinear electrostrictive actuators," *IEEE Transactions on Ultrasonics, Ferroelectrics, and Frequency Control*, 45(2), pp. 409-420, 1998.
- [22] F.T. Calkins, R.C. Smith and A.B. Flatau, "An energy-based hysteresis model for magnetostrictive transducers," ICASE Report 97-60; *IEEE Trans. Magn.*, submitted.
- [23] B.D. Cullity, *Introduction to Magnetic Materials*, Addison-Wesley, Reading, MA, 1972.
- [24] F.T. Calkins, "Design, analysis, and modeling of giant magnetostrictive transducers," PhD Dissertation, Iowa State University, Ames, IA, 1997.
- [25] R.C. Smith, "Modeling techniques for magnetostrictive actuators," Proceedings of the SPIE, Smart Structures and Materials 1997: Smart Structures and Integrated Systems, San Diego, CA, March 1997, Vol. 3041, pp. 243-253.
- [26] A.W. Leissa, *Vibration of Plates*, NASA SP-160, 1969, Reprinted by the Acoustical Society of America through the American Institute of Physics, 1993.
- [27] P.M. Prenter, *Splines and Variational Methods*, Wiley, New York, 1975.
- [28] D.C. Jiles and S. Hariharan, "Interpretation of the magnetization mechanism in Terfenol-D using Barkhausen pulse-height analysis and irreversible magnetostriction," *J. Appl. Phys.*, 67(9), pp. 5013-5015, 1990.